nature energy

Article

https://doi.org/10.1038/s41560-025-01958-8

Aqueous eutectic electrolytes suppress oxygen and hydrogen evolution for long-life Zn||MnO_2 dual-electrode-free batteries

Received: 26 May 2025

Accepted: 10 December 2025

Published online: 23 January 2026

Check for updates

Jinghan Li[1,4], Chang Li[1,4] ✉, Bo Liu[2], Yuzhang Li[2], Oleg Borodin[3] & Linda F. Nazar[1] ✉

Aqueous Zn^{2+}/Zn||MnO_2/Mn^{2+} batteries—operating via electrodeposition/dissolution—offer promising high-voltage, high-capacity grid-storage capabilities but require acidic conditions for MnO_2/Mn^{2+} conversion, and these induce problematic zinc corrosion. Here we present a global approach that identifies deep eutectic aqueous–organic electrolytes that strategically disrupt water's hydrogen-bonding network, simultaneously enhancing MnO_2 reversibility at the cathode while enabling stable zinc cycling at the anode without water decomposition. Such non-flammable electrolytes regulate the cation solvation structure and phase of the deposited MnO_2 and its morphology, promoting layered structures with enhanced ion-transport pathways that significantly improve stripping efficiency. These deep eutectics increase the oxygen evolution overpotential well above the MnO_2 deposition potential, which completely suppresses unwanted O_2 evolution. Moreover, they alter the local environment at the cathode interface to create localized interfacial pH gradients that influence critical processes, including optimizing proton transport and MnO_2 stripping. Our Zn^{2+}/Zn||MnO_2/Mn^{2+} dual-electrode-free battery achieves high Coulombic efficiency for extended cycling (>5,000 cycles) without external acid addition, advancing high-energy-density zinc–manganese battery development through rational electrolyte design.

Aqueous zinc-ion batteries have emerged as a cost-effective and safe energy storage technology for large-scale applications due to the zinc anode's high volumetric capacity (5,855 mAh cm^{-3}), aqueous electrolyte compatibility and abundance (52–83 ppm in the Earth's crust)[1–4]. However, intercalation-type aqueous zinc-ion batteries with conventional oxide cathodes (for example, MnO_2 (refs. 5,6) and V_2O_5 (refs. 7–9)) face challenges including sluggish Zn^{2+} diffusion in the oxide[10], competition between Zn^{2+} and proton intercalation[11,12], cathode dissolution[13,14] and structural transformation[15,16]. Recent research has focused on the Zn^{2+}/Zn||MnO_2/Mn^{2+} battery, the cathode of which undergoes an MnO_2 electrodeposition/dissolution mechanism with two-electron transfer (equation (1)), balanced by zinc plating/stripping at the anode (equation (2)):

$$\text{Cathode}: \ Mn^{2+}(aq.) + 2H_2O \leftrightarrow MnO_2(s) + 2e^- + 4H^+ \quad (1)$$

$$\text{Anode}: \ Zn^{2+}(aq.) + 2e^- \leftrightarrow Zn(s) \quad (2)$$

Such electrodissolution mechanism offers higher discharge voltage (2 V versus Zn^{2+}/Zn) and theoretical capacity (616 mAh g^{-1}) than oxide-intercalation analogues[17–22].

[1]Department of Chemistry and the Waterloo Institute for Nanotechnology, University of Waterloo, Waterloo, Ontario, Canada. [2]Department of Chemical and Biomolecular Engineering, University of California, Los Angeles, Los Angeles, CA, USA. [3]Battery Science Branch, Energy Sciences Division, DEVCOM Army Research Laboratory, Adelphi, MD, USA. [4]These authors contributed equally: Jinghan Li, Chang Li. ✉e-mail: c553li@uwaterloo.ca; lfnazar@uwaterloo.ca

Traditional approaches achieve MnO_2 dissolution on discharge by adding strong acids (equation (1), going to the left)[23–25]. Chao et al.[26] demonstrated highly reversible deposition/dissolution in 1 M $ZnSO_4$ + 1 M $MnSO_4$ + 0.1 M H_2SO_4 electrolyte, achieving 2 V discharge. Similarly, sulfuric acid-based electrolytes enabled MnO_2/Mn^{2+} conversion with hydrogen and other metal anodes, achieving high energy and power densities[27–29]. A weak Brønsted acid (acetic acid) was used to form a buffered solution that assists the proton-coupled electron transfer reaction[30,31]. However, the introduction of acid causes severe zinc anode corrosion, limiting long-term performance. Although decoupled batteries with ion-selective membranes prevent corrosion and allow full MnO_2 utilization, their application is limited by the costly, complex set-up required[32,33].

Recent studies have therefore explored systems without externally added acids, utilizing substrate and electrolyte engineering. Dai et al.[34] developed a multivalent manganese oxide cathode, delivering a 2-V discharge voltage plateau in 2 M $ZnSO_4$ + 0.5 M $MnSO_4$. However, the plateau was limited to low current densities with Zn^{2+}/H^+ intercalation at lower voltages. Anion and cation chemistry was explored to optimize ion association properties, suppress side reactions and enhance MnO_2/Mn^{2+} redox kinetics[35,36]. Li et al.[37] modified a conventional electrolyte (1 M $ZnSO_4$ + 1 M $MnSO_4$) with 0.1 mM surfactant, depositing layered δ-MnO_2 and achieving high stripping efficiency in their dual-electrode-free battery. Despite this exciting progress, the oxygen evolution reaction (OER; equation (3)) at 2.3 V versus Zn^{2+}/Zn and resultant electrolyte depletion remain concerns.

$$\mathrm{OER}:\ H_2O(\mathrm{aq.}) \rightarrow \frac{1}{2}O_2(\mathrm{g}) + 2H^+ + 2e^- \qquad (3)$$

Additionally, protons generated during MnO_2 deposition or the OER (Fig. 1a and equations (1) and (3)) can migrate to the anode, corroding zinc.

Mixing H_2O with certain non-aqueous solvents results in eutectic solutions that disrupt water hydrogen bonding[38], expanding the stability window of electrolytes and improving zinc reversibility[39,40]. We and others reported that sulfolane (SL) reduces water activity, enabling efficient zinc stripping/plating with long-term stability[41,42]. Other high-donor-number solvents (for example, succinonitrile (SN)[43], ethylene glycol[44], dimethylsulfoxide (DMSO)[45] and acetamide[46]) modify Zn^{2+} solvates and form hydrogen bonds with water. Despite their promise for controlling water activity[47], cosolvent approaches for metal oxide electrodeposition/stripping at cathodes have not been fully explored, leaving vast, tunable composition ranges with substantial potential.

Here we report a universal strategy whereby eutectic electrolytes stabilize $Zn^{2+}/Zn||MnO_2/Mn^{2+}$ cells without external acids. We find that DMSO/water, SL/water and, in particular, mixed SL/DMSO/water systems establish MnO_2 phase regulation, and exhibit excellent anodic stability and localized pH control. Holistically, these factors significantly enhance MnO_2/Mn^{2+} reversibility (Fig. 1b). The hybrid electrolytes regulate cation solvation and promote layered δ-MnO_2 formation with expanded interlayer spacing that enables fast proton diffusion, contrasting with typical dense tunnelled structures deposited from conventional aqueous electrolytes[48–51]. The organic components alter interfacial chemistry by interrupting proton transfer pathways and confining in situ-generated protons near the cathode[42], while simultaneously suppressing the oxygen and hydrogen evolution reactions (OER and HER). Consequently, dual-electrode-free $Zn^{2+}/Zn||MnO_2/Mn^{2+}$ batteries with a hybrid electrolyte deliver average coulombic efficiency (CE) >95% and achieve 90% capacity retention after 5,000 cycles at a viable capacity, demonstrating potential for low-cost, scalable energy storage applications.

The electrochemical performance of $Zn^{2+}/Zn||MnO_2/Mn^{2+}$ cells in hybrid electrolytes

The hybrid electrolytes comprise 1 M $Zn(OTf)_2$ + 0.5 M $MnCl_2$ dissolved in different organic/water cosolvent deep eutectics. We examined different weight percentages of organic solvents: 0SL–90SL, 20DMSO–70DMSO and 20SN–90SN, representing percentages of SL, DMSO and SN, respectively. These solvents were selected for their electron-donating (measured by their donor number) and hydrogen-accepting properties, which affect their interaction with the cations and water's hydrogen-bond network, respectively. The donor number of DMSO (29.8) is twice that of SL (14.8) or SN (15), while both DMSO and SL are strong hydrogen-bonding acceptors (HBAs) versus the weak HBA ability of SN[38]. This makes it possible to correlate these characteristics governing cation solvation and hydrogen-bond formation in the eutectic solvents with electrochemical behaviour.

Differential scanning calorimetry (DSC; Supplementary Fig. 1) identified 70SL, 70DMSO and 90SN as eutectic compositions with the lowest melting points. Using SL as a representative, increasing the SL/water ratio led to significant electrolyte structural changes. Fourier transform infrared (FTIR) spectroscopy (Supplementary Fig. 2) shows the water O–H stretching band initially blue-shifted from 0SL to 70SL then red-shifted in 90SL, indicating a phase transition at 70SL where water's hydrogen bonding is most disrupted[41,52]. This is consistent with DSC results (Supplementary Fig. 1a), showing continuous melting point decrease from 0SL to 70SL, followed by an increase at 90SL.

These structural changes directly influenced the electrochemical performance of dual-electrode-free $Zn^{2+}/Zn||MnO_2/Mn^{2+}$ cells with copper and graphite felt as the current collectors for anode and cathode, respectively. Following initial screening (Supplementary Figs. 3–5), 70SL, 70DMSO and 70SN (with widely differing HBA characteristics) were selected and compared to a benchmark 'baseline' electrolyte (BE), 1 M $ZnSO_4$ + 1 M $MnSO_4$ (refs. 26,37,53). Figure 2a shows the full cell charged at 2.3 V for 0.5 mAh cm^{-2} and galvanostatically discharged at 5 mA cm^{-2} to 1 V. The hybrid electrolytes demonstrated high discharge capacities with ~90% CE for the second cycle, whereas the BE cell showed a lower CE of 78%. 70DMSO demonstrated the longest cycling lifetime by far, with an 90% average CE and 80% capacity retention after 3,500 cycles (Fig. 2b), while 70SL achieved the highest average CE of 97%, retaining 80% of its capacity after 800 cycles. In contrast, 70SN (weakest HBA) experienced continuous capacity decay over 250 cycles, while the BE cell failed after 60 cycles with a maximum CE of 87%. At a higher areal capacity (2 mAh cm^{-2}, Fig. 2c,d), 70DMSO exhibited a lower CE of 77% despite its longer cycling lifetime. 70SL achieved a higher average CE of 95%, retaining 85% capacity after 250 cycles, while the BE showed <68% CE with a significantly limited cycle life. The lower CE in 70DMSO is due to slight oxidation of DMSO to $DMSO_2$ during charging at high potential (Supplementary Fig. 6). The lower discharge voltage is attributed to 70DMSO's higher viscosity causing larger voltage polarization (Supplementary Fig. 7).

Recognizing the complementary advantages of SL and DMSO—the higher CE of SL and the superior cycling stability of DMSO—we developed a ternary-solvent electrolyte containing H_2O:DMSO:SL (3:3:4, wt%). This optimized SL/DMSO electrolyte successfully extends the cycling lifetime beyond either individual system, achieving 95% average CE at 0.5 mAh cm^{-2} with 90% capacity retention after 5,000 cycles (Fig. 2e). SL/DMSO also improved performance at 2 mAh cm^{-2}, maintaining 90% CE for 300 cycles (Fig. 2f) and yielding an energy density of 167 Wh kg^{-1} (Supplementary Table 1). The cell was also cycled at a more moderate discharge rate of 1 C (current density, 1 mA cm^{-2}) at a capacity of 1 mAh cm^{-2}, maintaining 90% CE after 200 cycles (Supplementary Fig. 8). Furthermore, the eutectic electrolytes enable extended operating temperature ranges (Supplementary Fig. 9). At -15 °C, SL/DMSO cell achieved over 600 cycles with 97% CE at 0.5 mAh cm^{-2} and 200 cycles with 2 mAh cm^{-2}, demonstrating the unique properties of eutectic systems below 0 °C.

Cathode characterization of the charged product

To understand factors underlying these different electrochemical signatures, we performed X-ray diffraction (XRD) analysis to investigate

https://doi.org/10.1038/s41560-025-01958-8

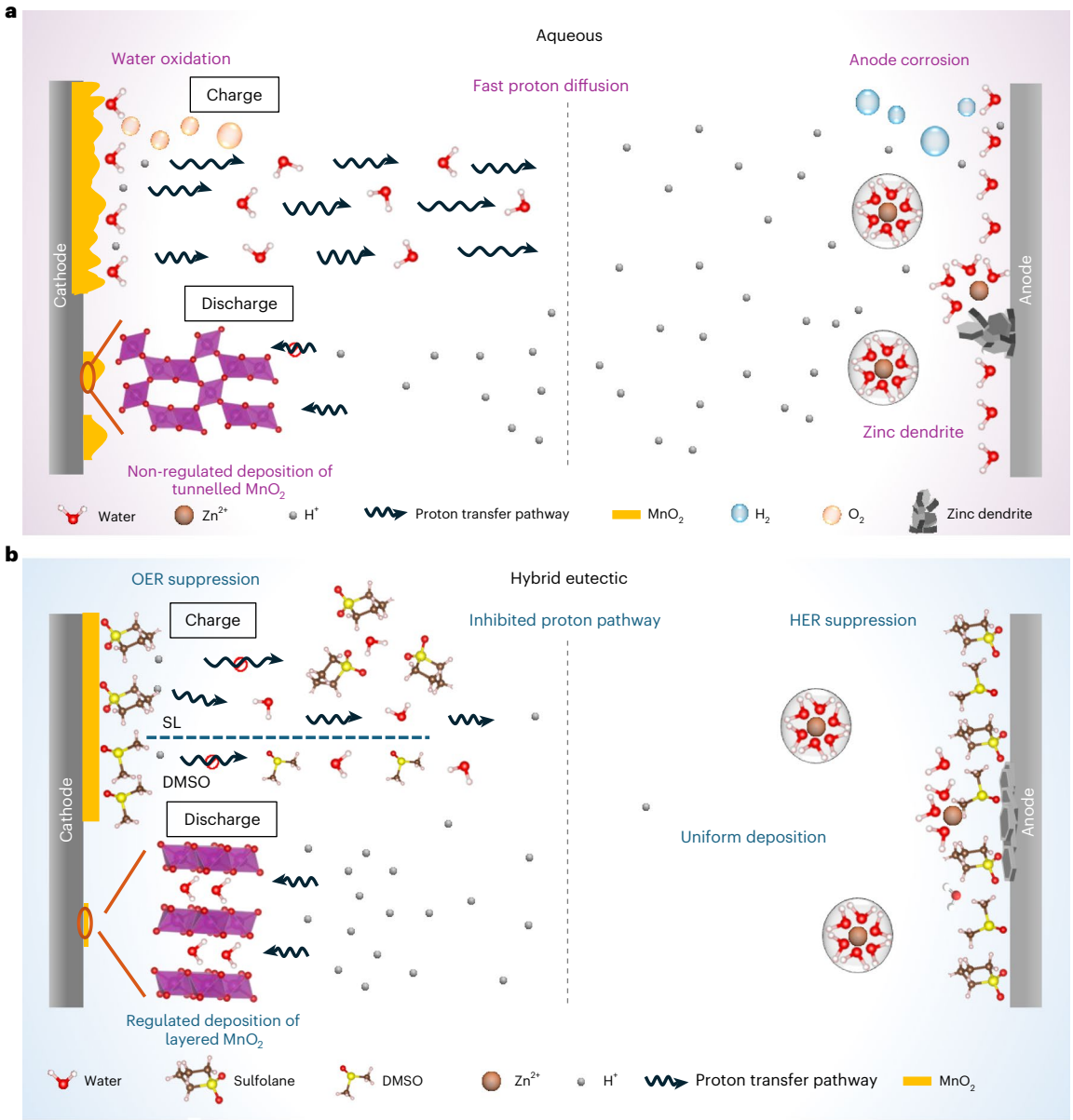


Fig. 1 | Schematic representation of a Zn^{2+}/Zn||MnO_2/Mn^{2+} battery. a, Reaction mechanism and proton transfer pathway in Zn^{2+}/Zn||MnO_2/Mn^{2+} battery with the baseline aqueous electrolyte. **b**, Hybrid eutectic electrolytes with SL and DMSO.

the nature of the MnO_2 deposits (Fig. 3a). Despite broad and overlapping reflections, our results show that electrolyte composition regulates MnO_2 deposition phases. In 70SL, birnessite (δ-MnO_2)—identified by its unique low-angle interlayer spacing of 7.2 Å—coexists with ε-MnO_2 but is more prominent in 70DMSO and SL/DMSO. In the BE, however, only conventional 'electrolytic' ε-MnO_2 was identified, whereas δ-MnO_2 is absent, consistent with literature findings[18,19,37]. The same was observed for 70SN. This correlates with the enhanced cycling lifetimes in DMSO and SL, whereas 70SN exhibits poor reversibility despite its eutectic nature, as discussed later. Cryogenic electron microscopy (cryo-EM; Fig. 3b) confirmed these phases, showing the (100) plane of ε-MnO_2 in the BE with a 2.4-Å interplanar spacing and a larger 7.3-Å spacing in 70DMSO and SL/DMSO, corresponding to the (002) plane of δ-MnO_2. Due to the thick compact MnO_2 layers in 70SL (Supplementary Fig. 10) and its mixed-phase nature, we only identified the lattice fringes of ε-MnO_2 in direct transmission electron microscopy (TEM) imaging. However, the selected-area electron diffraction pattern of MnO_2 deposited in 70SL displays concentric rings indexed to the (006), (201), (331) and (119) planes of δ-MnO_2—matching the pattern observed in 70DMSO—while the BE shows a distinctly different pattern with lattice spacings indexed to the (100), (002), (101) and (102) planes of ε-MnO_2. Scanning TEM energy-dispersive X-ray spectroscopy (STEM-EDS) mapping reveals uniform manganese and oxygen distribution in all deposits. Notably, no zinc signal was detected in δ-MnO_2, suggesting H_3O^+ may occupy the interlayer spaces (given the absence of other cations in the electrolyte)[54], effectively promoting proton diffusion kinetics in the layer. Similar phase regulation has been reported in aqueous electrolytes containing surfactant additives[37], suggesting the crucial role of electrolyte additives and the interfacial chemistry in dictating MnO_2 crystallization. TEM surveys from various sample regions (Supplementary Figs. 11–14) and high-resolution TEM statistics for MnO_2 phase analysis in different electrolytes, collected over 50 independent lattice spacing measurements per electrolyte importantly confirm the nature of these phases (Supplementary Fig. 15).

Notable morphological differences were observed in different electrolytes. TEM images (Fig. 3b) reveal flower-like structures in the

https://doi.org/10.1038/s41560-025-01958-8

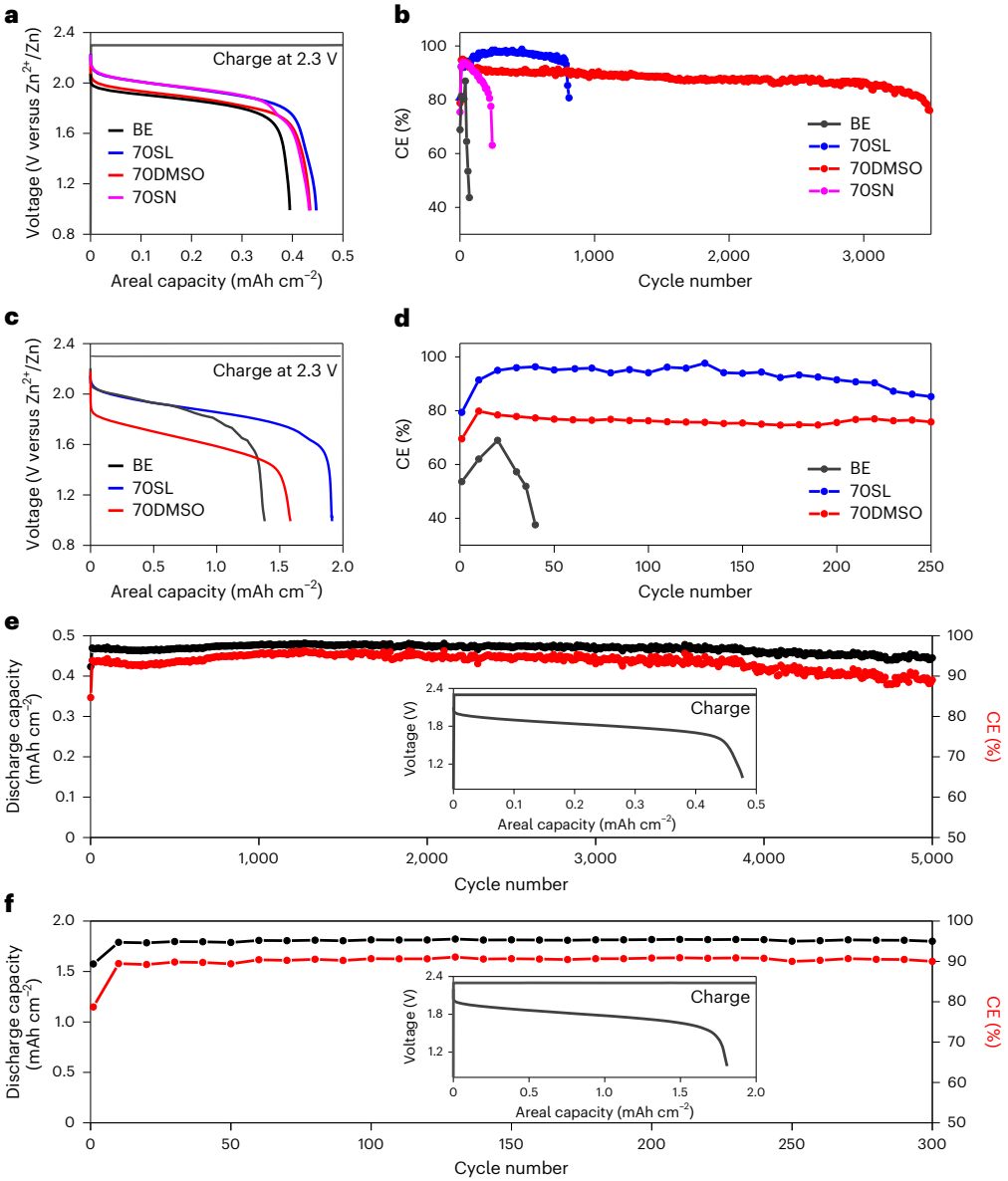


Fig. 2 | Electrochemical performance of the Zn^{2+}/Zn||MnO_2/Mn^{2+} full cell. a, Voltage profiles for full cells charged at 2.3 V for 0.5 mAh cm^{-2} and galvanostatically discharged at 5 mA cm^{-2} in different electrolytes of the second cycle. **b**, CE of full cells in different electrolytes at 0.5 mAh cm^{-2}. **c**, Voltage profiles of full cells in 70SL, 70DMSO and the BE charged to 2 mAh cm^{-2} and discharged at 12 mA cm^{-2}. **d**, CE of full cells at 2 mAh cm^{-2}. **e**, Voltage profiles and CE of full cells in SL/DMSO ternary electrolyte charged to 0.5 mAh cm^{-2} and discharged at 5 mA cm^{-2}. **f**, Voltage profiles and CE of full cells in SL/DMSO ternary electrolyte charged to 2 mAh cm^{-2} and discharged at 12 mA cm^{-2}.

BE, whereas hybrid electrolytes exhibit a more uniform mesh-like structure. SEM images (Fig. 4) show that MnO_2 nucleates into spheres in the BE, while thin fibres form a more uniform, porous layer in hybrid electrolytes, consistent with that previously observed for δ-MnO_2 (ref. 55). Moreover, additional cracks and grooves observed in 70DMSO and SL/DMSO deposits create high-surface-area structures that provide additional proton transport pathways, abundant reaction sites and faster insertion kinetics, thus accounting for the improved reversibility and enhanced MnO_2 dissolution. Furthermore, MnO_2 in DMSO-containing electrolytes exhibits decreased crystallinity (Supplementary Fig. 16), characteristic of highly defective birnessite, while long-range crystallinity was evident in the other two electrolytes. These structural variations significantly influence electrochemical performance[56]. We expect that layered δ-MnO_2 deposited in the hybrid electrolytes will facilitate more efficient proton diffusion than tunnelled ε-MnO_2 (refs. 48–50,57) and offer slightly higher electronic conductivity (4 mS m^{-1} versus 2 mS m^{-1} for ε-MnO_2)[58], thereby improving MnO_2 reduction kinetics during discharge. The defect-ridden birnessite in DMSO also reduces adhesion to the carbon fibre substrate, preventing rigid thick deposits and limiting residual MnO_2 accumulation[35], thereby improving cyclability and extending battery lifetime[59]. The ternary electrolyte successfully preserves DMSO's phase and morphology selectivity, forming widely accessible δ-MnO_2 while maintaining the stability of SL—creating a synergistic effect that enables both optimal phase formation and extended cycling.

Cationic solvation structure: influence on MnO_2 deposition

Zn^{2+} and Mn^{2+} solvation structures play crucial roles during charge in regulating deposition as revealed by Raman spectroscopy, density functional theory (DFT) and molecular dynamics (MD) simulations. Raman spectra (Fig. 5a) reveal a contact ion pair peak (Zn–O=S) in

https://doi.org/10.1038/s41560-025-01958-8

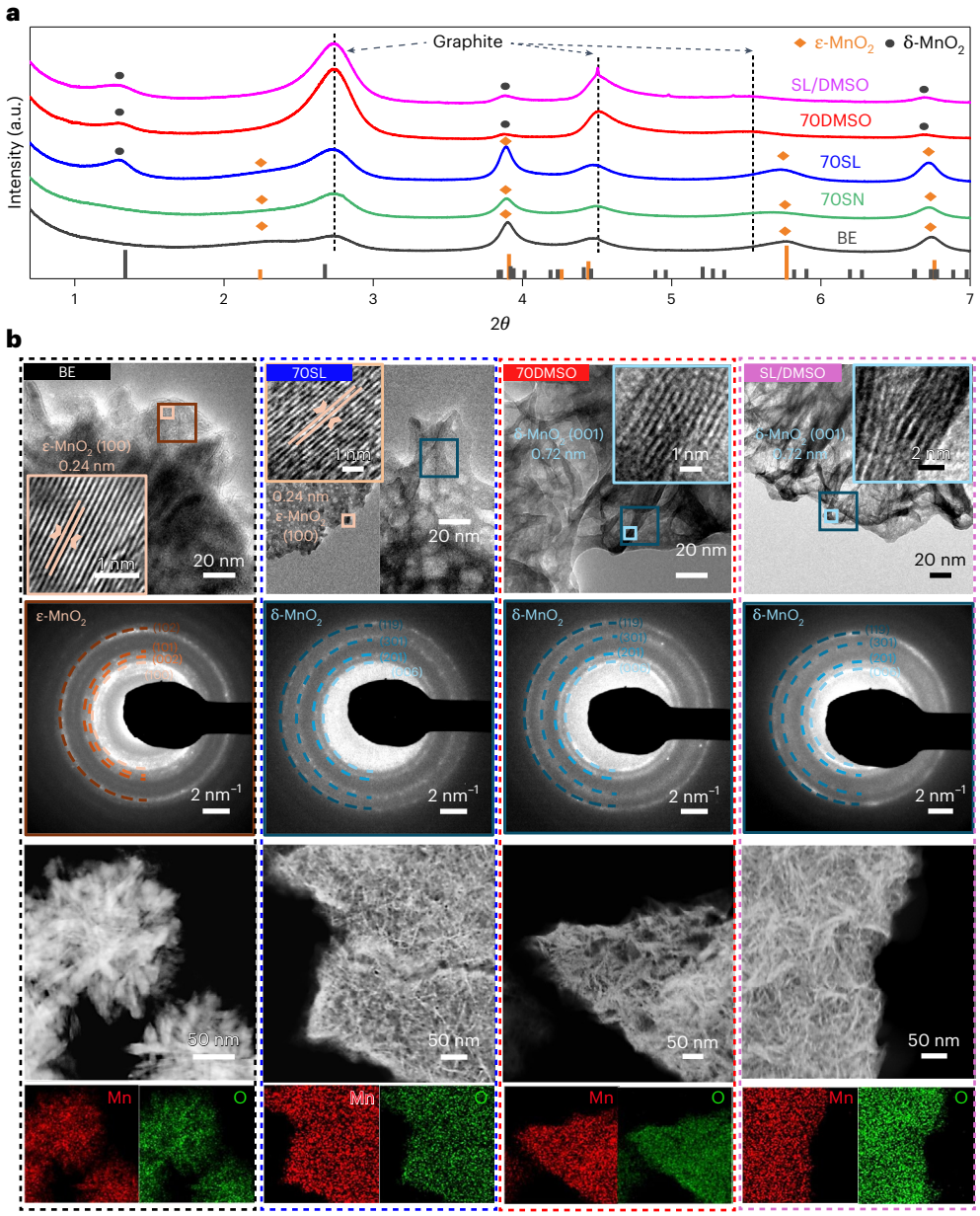


Fig. 3 | Characterization of the deposition product on the cathode. **a**, Synchrotron XRD patterns acquired at $\lambda = 0.165$ Å of MnO_2 deposited in different electrolytes. The isolated low-angle reflections at $2\theta = 1.3°$ (7.2 Å) and $2\theta = 2.3°$ (4.2 Å) are characteristic of layered δ-MnO_2 and ε-MnO_2, respectively, while the other reflections are highly overlapped. Reference JCPDS patterns for ε-MnO_2 and δ-MnO_2 are numbers 030-0820 and 080-1098, respectively. **b**, Cryo-TEM images of MnO_2 deposited in BE (first, left-most column), 70SL (second column), 70DMSO (third column) and SL/DMSO (fourth, right-most column) with interlayer spacings labelled. STEM-EDS mapping of the charged cathodes at 2 mAh cm^{-2} and their selected-area electron diffraction patterns are also shown.

crystalline $Zn(OTf)_2$ at 1,034 cm^{-1} (ref. 60), while in organic electrolytes the OTf^- $\delta_s(CF_3)$ and $\nu_s(SO_3)$ bands at 750–755 cm^{-1} and 1,024–1,034 cm^{-1} were assigned to the solvent-separated ion pairs[61]. When dissolved in water ($Zn(OTf)_2/H_2O$), $Zn^{2+}(H_2O)_6$ formation causes anion peaks to red-shift with positions consistent with solvent-separated ion pair assignments[62,63]. Adding SL ($Zn(OTf)_2$/70SL) does not significantly change their positions. Similarly, SL peaks remain unchanged upon salt addition, suggesting minimal SL solvation with cations in the dual-cation electrolyte. The cation solvation structures are predominantly formed by anions and water, as established in our previous $Zn(OTf)_2$–SL–water study[41].

However, 70DMSO exhibits different solvation (Fig. 5b). The S=O stretching mode of DMSO around 1,040 cm^{-1} continues red-shifting from the single- to the dual-salt system, indicating increased DMSO participation in cation solvation. Analysis of the water –OH stretching region supports this (Fig. 5c). In 70SL solvent, the 3,525 cm^{-1} peak red-shifted to lower frequencies with individual salt, confirming water participates in Zn^{2+} and Mn^{2+} solvation shells[41]. The peaks then return to 3,517 cm^{-1} with both salts present, reflecting collaborative component interactions. In 70DMSO, the –OH stretching peak shifts minimally from pure solvent (3,425 cm^{-1}) to $MnCl_2$/70DMSO (3,421 cm^{-1}), contrasting with substantial shifts observed in 70SL and indicating limited water–Mn^{2+} interaction. Addition of $Zn(OTf)_2$ to $MnCl_2$/70DMSO induces a more significant blue-shift, suggesting progressive water exclusion from cation coordination[64]. Notably, 1 M $Zn(OTf)_2$ does not dissolve in 70DMSO solvent, further suggesting unique preferential solvation in the dual-salt DMSO system. This is further supported by Raman spectra

https://doi.org/10.1038/s41560-025-01958-8

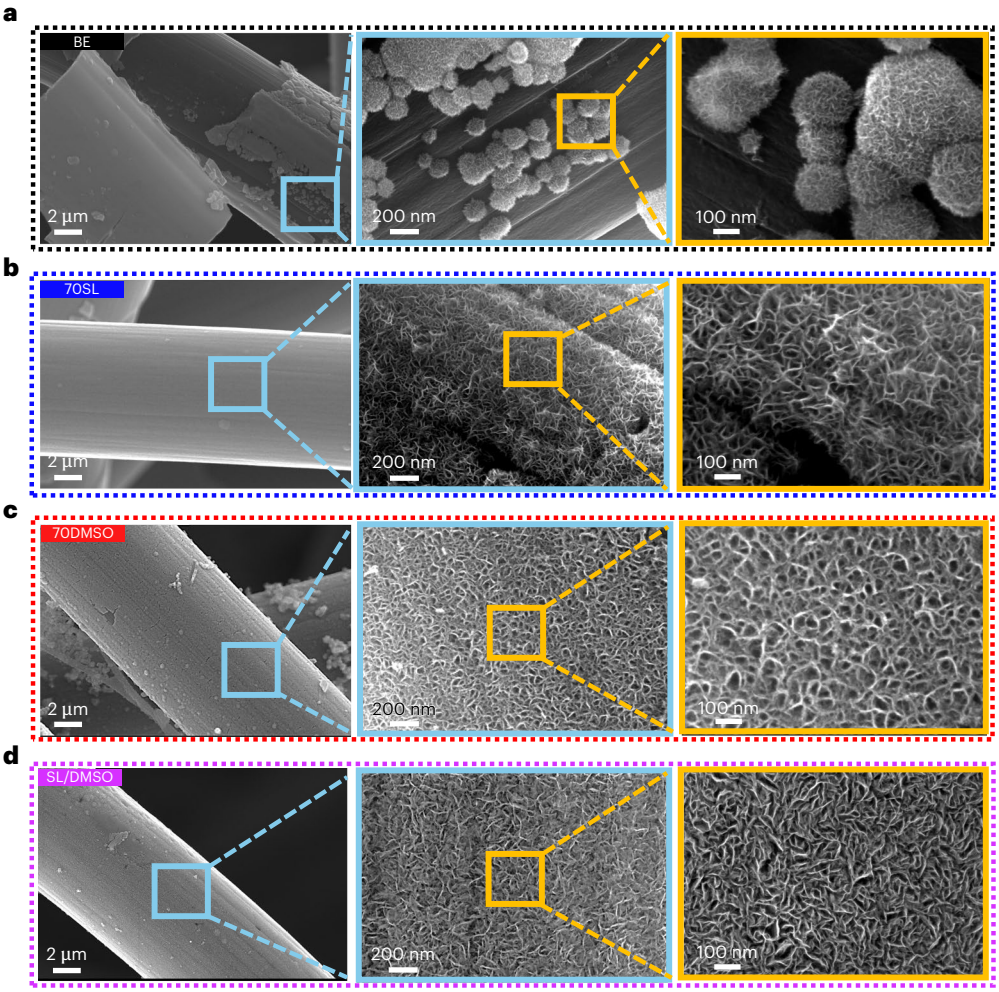


Fig. 4 | Differences of MnO_2 morphology in different electrolytes. a–d, SEM images of 0.5 mAh cm^{-2} MnO_2 deposited in the BE (**a**) and in 70SL (**b**), 70DMSO (**c**) and SL/DMSO (**d**).

in the –OH stretching region for SL/DMSO (Supplementary Fig. 17) where the water peak shifts significantly upon $Zn(OTf)_2$ addition but remains unchanged with $MnCl_2$.

Near-complete dissociation of Mn^{2+} and Zn^{2+} from OTf^- observed in MD simulations of the SL/DMSO/H_2O–$Zn(OTf)_2$–$MnCl_2$ electrolyte supports Raman measurements. Radial distribution function (RDF) analysis (Fig. 5d,e) demonstrates that DMSO participates in Mn^{2+} and Zn^{2+} solvation by displacing water, while SL rarely binds to these cations: the first peak RDF magnitudes follow the order: Mn–O(DMSO) > Mn–Ow(H_2O) > Mn–Cl > Mn–O(SL) > Mn–O(OTf) and Zn–Cl > Zn–O(DMSO) > Zn–Ow > Zn–O(SL) > Zn–O(OTf), where w denotes water. Moreover, MD simulations at 363 K found that the residence time of O(DMSO) around Mn^{2+} is five times longer than that of Mn^{2+}–Ow and O(SL), indicating significantly slower exchange dynamics of DMSO compared with water and SL in the Mn^{2+} solvation shell. This unique DMSO-participating Mn^{2+} solvation structure induces a higher desolvation barrier during MnO_2 deposition, potentially resulting in poorly crystalline layered MnO_2 deposits in DMSO-containing electrolytes that subsequently facilitates dissolution during discharge as discussed above. DFT cluster-continuum calculations of Mn^{2+} and Zn^{2+} solvates in implicit solvent and MD simulations are discussed in Supplementary Note 1 and Supplementary Tables 3 and 4. Interestingly, DFT calculations predict stronger Zn–Cl^- ion pairing than Mn–Cl^- in aqueous environments, and MD simulations show significant Zn^{2+}–Cl^- affinity resulting in 0.8 Cl^- per Zn^{2+} on average, while much weaker Mn^{2+}–Cl^- coordination yields only 0.2 Cl^- per Mn^{2+}.

Hydrogen-bonding characterization (Fig. 5f) shows significantly stronger DMSO–H_2O binding energy (~40 kJ mol^{-1}) than H_2O–H_2O (~20 kJ mol^{-1}) and SL–H_2O (~33 kJ mol^{-1}) (Supplementary Fig. 18), resulting in a more pronounced DMSO–H_2O RDF peak compared with the H_2O–H_2O and H_2O–O(SL) peaks, indicating DMSO's superior ability to perturb water's hydrogen-bonding network. This results in formation of interpenetrating water chains and channels shown as red isosurfaces in Fig. 5g that participate in solvation of both Cl^- and OTf^- anions and cations (Fig. 5h and Supplementary Figs. 19 and 20).

Enhanced MnO_2 deposition/dissolution reversibility in hybrid electrolytes

X-ray photoelectron spectroscopy (XPS) and electrochemical impedance spectroscopy (EIS) studies were conducted on cathodes to probe the cathode surface chemistry. XPS manganese 2*p* spectra (Fig. 6a–d) confirm MnO_2 deposition on the first charge (1C) cycle in all electrolytes. After discharge (1D), almost complete MnO_2 dissolution was observed in hybrid electrolytes, while residual MnO_2 was detected in the BE. EIS analysis (Fig. 6e–h) revealed primarily diffusion-controlled reactions before cycling in all electrolytes due to the absence of redox active species on pristine graphite. However, after the tenth cycle in the BE, distinguishable semicircles appeared in the Nyquist plot and continued growing during cycling, indicating MnO_2 accumulation. This

https://doi.org/10.1038/s41560-025-01958-8

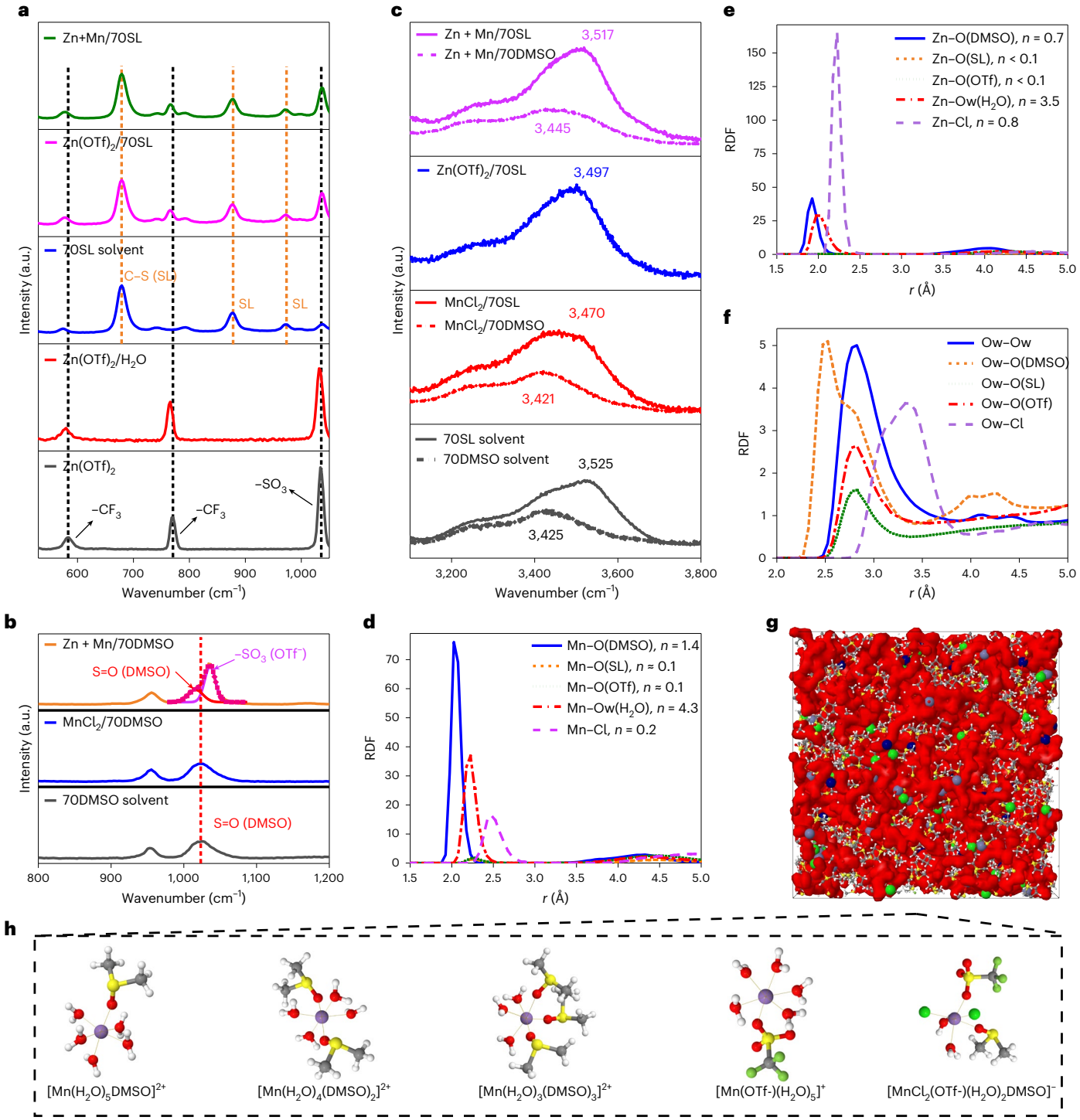


Fig. 5 | Cationic solvation structure. a, Raman spectra of $Zn(OTf)_2$ salt in different SL solutions in the wavenumber region of $-CF_3$ deformation and $-SO_3$ stretching bands. Orange dotted lines represent signals from SL, and black dotted lines represent signals from triflate anion. **b**, Raman spectra comparing different 70DMSO systems. The red dotted line indicates the S=O stretching mode in DMSO. The peak in Zn + Mn/70DMSO is fitted with the S=O peak of DMSO and the $-SO_3$ peak of $Zn(OTf)_2$. **c**, Raman spectra of different solutions in the –OH stretching band of water. The peak wavelengths of the –OH stretching bands in different solutions are labelled. **d**–**f**, RDFs from MD simulations of the SL/DMSO electrolyte at 90 °C with the metal coordination numbers *n* shown in the legend for a 3-Å coordination shell for Mn^{2+} (**d**), Zn^{2+} (**e**), and oxygen of water (**f**). **g**, A snapshot of MD simulation box highlights water using red isosurfaces and ions shown as large spheres: Cl, green; Mn, dark blue; Zn, grey. **h**, Some representative Mn^{2+} clusters in the SL/DMSO model using jmol colour scheme: H, white; O, red; S, yellow; C, grey; Cl, light green; F, dark green; Mn, purple.

increases charge transfer resistance (R_{CT}) at the cathode. In contrast, the smaller impedance increase in DMSO-containing electrolytes is attributed to surface electrolyte oxidation and formation of a passivation layer. No significant R_{CT} was observed in 70SL, suggesting nearly complete MnO_2 dissolution during each cycle, consistent with the high CE observed in the full cell (Fig. 2). SEM images further supported this, showing relatively clean carbon fibres after discharge in hybrid electrolytes (Fig. 6i–l and Supplementary Fig. 21), in contrast to

https://doi.org/10.1038/s41560-025-01958-8

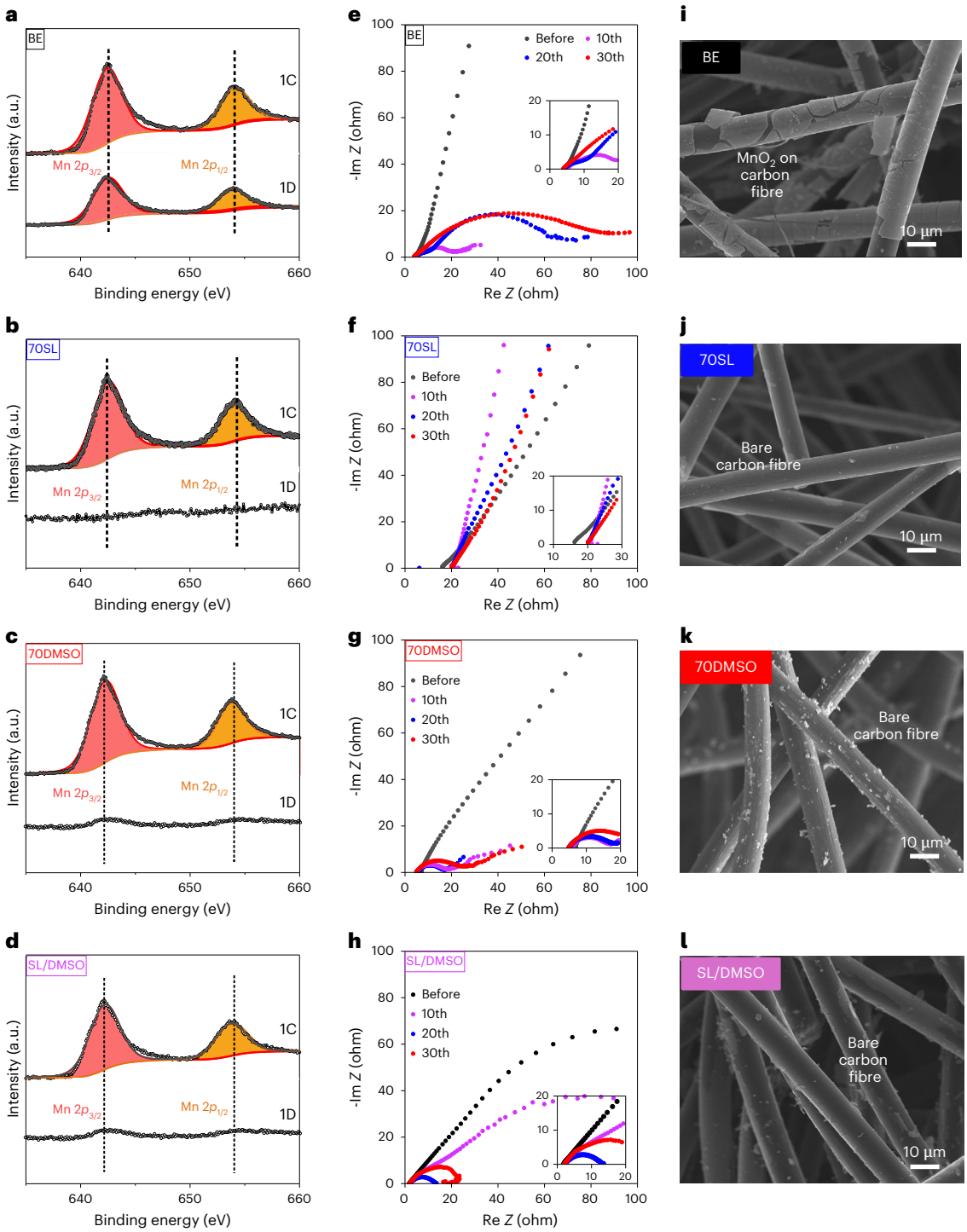


Fig. 6 | Reversibility of MnO_2 deposition and dissolution. a–**d**, XPS manganese 2*p* spectra of cathodes cycled at 0.5 mAh cm^{-2} in the BE (**a**) and in 70SL (**b**), 70DMSO (**c**) and SL/DMSO (**d**) after the first charge and discharge. **e**–**h**, EIS analysis of the full cell before cycling and after different discharge cycles in the BE (**e**) and in 70SL (**f**), 70DMSO (**g**) and SL/DMSO (**h**). **i**–**l**, SEM images of cathodes after ten cycles in discharge at 0.5 mAh cm^{-2} in the BE (**i**) and in 70SL (**j**), 70DMSO (**k**) and SL/DMSO (**l**). The solids observed at the surface of carbon fibres in 70DMSO and SL/DMSO are $DMSO_2$ formed after DMSO oxidation, confirmed by FTIR spectroscopy and gas chromatography–mass spectrometry (Supplementary Fig. 6).

residual MnO_2 layers in the BE. Such incomplete MnO_2 dissolution in the BE is more pronounced at a higher areal capacity and after prolonged cycling (Supplementary Figs. 22 and 23 and Supplementary Table 2). The compact layer formed on the cathode surface in the BE exacerbates reaction irreversibility by impeding proton diffusion and charge transfer[65,66], whereas the hybrid electrolytes minimize such residue accumulation, effectively mitigating capacity degradation.

Dynamic pH evolution induced by MnO_2 deposition/dissolution

To probe the mechanistic basis for why certain organic solvents improve electrochemical performance, we examined each compound's ability to disrupt water bonding and activity. While both SL and DMSO are strong HBAs and modify hydrogen-bond networks in zinc-based aqueous batteries, they do so through fundamentally

https://doi.org/10.1038/s41560-025-01958-8

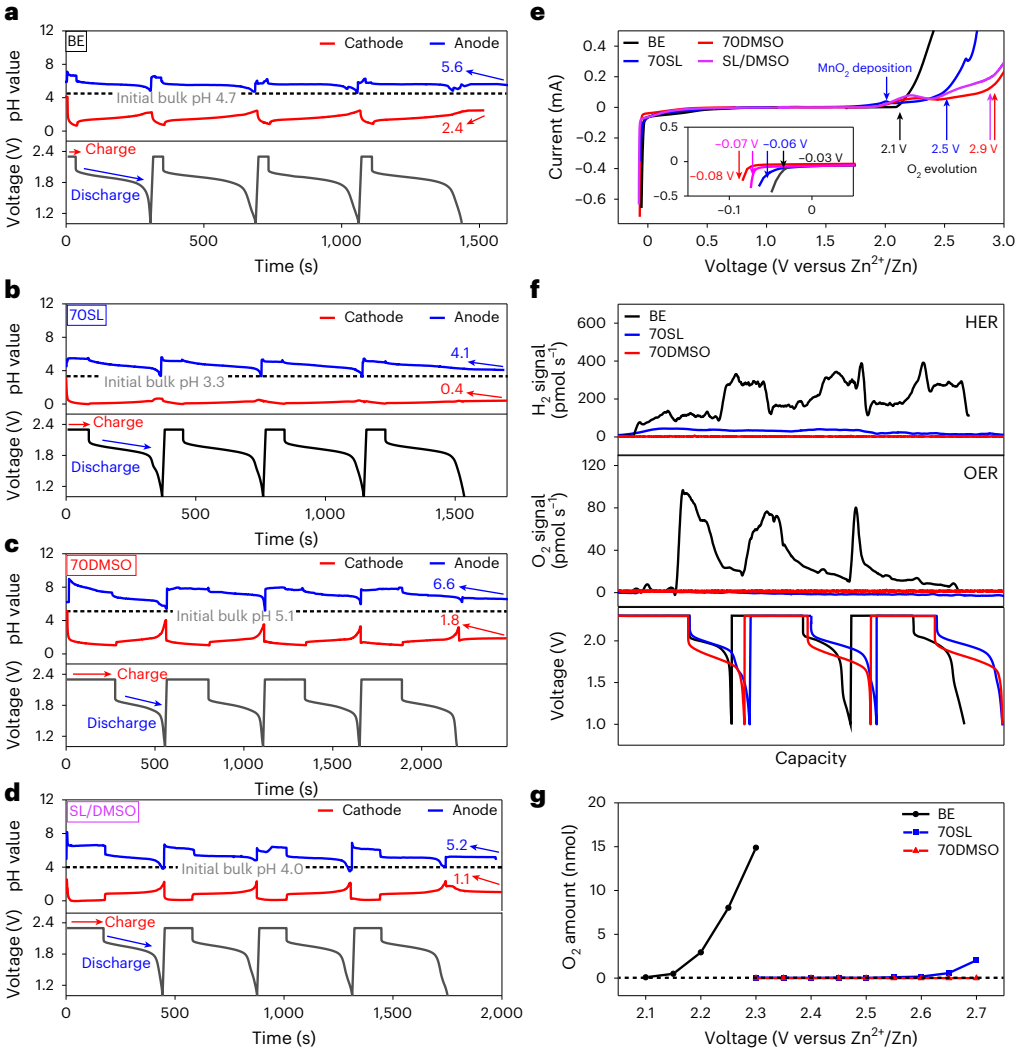


Fig. 7 | pH and gas evolution during cycling. a–**d**, Voltage profiles and pH evolution at both electrodes upon the initial four cycles in the BE (**a**) and in 70SL (**b**), 70DMSO (**c**) and SL/DMSO (**d**). **e**, LSV of the BE and 70SL, 70DMSO and SL/DMSO. **f**, DEMS signals of oxygen and hydrogen evolution in different electrolytes for the initial three cycles. **g**, Amount of oxygen evolved during the first cycle as a function of charging voltage in different electrolytes.

different mechanisms[38]. DMSO reconstructs hydrogen bonds by disrupting water–water hydrogen bonds and forming new networks that block proton transport pathways[45,67]. SL, on the other hand, acts as a crowding agent, creating isolated water clusters that reduce water activity[41,68]. FTIR spectra (Supplementary Fig. 24) comparing 70SL and 70DMSO to the pure aqueous electrolyte (1 M $Zn(OTf)_2$ + 0.5 M $MnCl_2$ in water) reflect different mechanisms because the electrolytes disrupt water's hydrogen-bond network differently. The –OH stretching mode significantly blue-shifted in 70SL while remaining relatively unchanged in 70DMSO, corresponding to hydrogen-bond network reconstruction in 70DMSO and a crowding phenomenon in 70SL. These mechanistic differences significantly impact important electrochemical processes such as proton transport and HER/OER side reactions.

We conducted operando pH measurements[69] to monitor pH evolution on the electrode surfaces. Electrochemical MnO_2 deposition/dissolution generates/consumes protons at the cathode/electrolyte interface (equation (1)), leading to significant interfacial and bulk pH fluctuations. During charge in all electrolytes (Fig. 7a–d), cathode pH decreased immediately and continued dropping gradually throughout the process, indicating rapid and continuous proton generation during MnO_2 deposition. During discharge, cathode pH increased as protons were consumed during MnO_2 dissolution. Subsequent cycles exhibited similar trends.

The pH changes in all electrolytes followed similar patterns; however, the extent of decrease differed. At equilibrium after cycling, the cathode stabilized at pH 0.4 in 70SL, at pH 1.8 in 70DMSO and at pH 1.1 in SL/DMSO, versus pH 2.4 in the BE. The consistently lower pH in hybrid electrolytes indicates a significantly higher proton concentration at the cathode which facilitates proton-coupled electron transfer and enhances MnO_2 dissolution (equation (1)). Despite higher proton concentration at the cathode, the anode pH in 70DMSO remained close to neutral, while in 70SL and SL/DMSO it became mildly acidic. Differential electrochemical mass spectrometry (DEMS) analysis shows that anodes are relatively unaffected, as 70DMSO exhibits a reduced HER (equation (4)) in the hybrid electrolytes versus the BE, attributed to reduced H^+ activity and solid–electrolyte interphase formation in the eutectic electrolytes (discussed below).

$$\text{HER}: 2H^+ + 2e^- \rightarrow H_2(g) \quad (4)$$

These findings highlight the role of the hybrid electrolytes in maintaining favourable pH conditions that support enhanced electrochemical performance.

Beyond pH regulation, the hybrid electrolytes exhibited a surprisingly enhanced electrochemical stability window. Linear sweep voltammetry (LSV; Fig. 7e) shows a higher OER onset potential of 2.9 V

https://doi.org/10.1038/s41560-025-01958-8

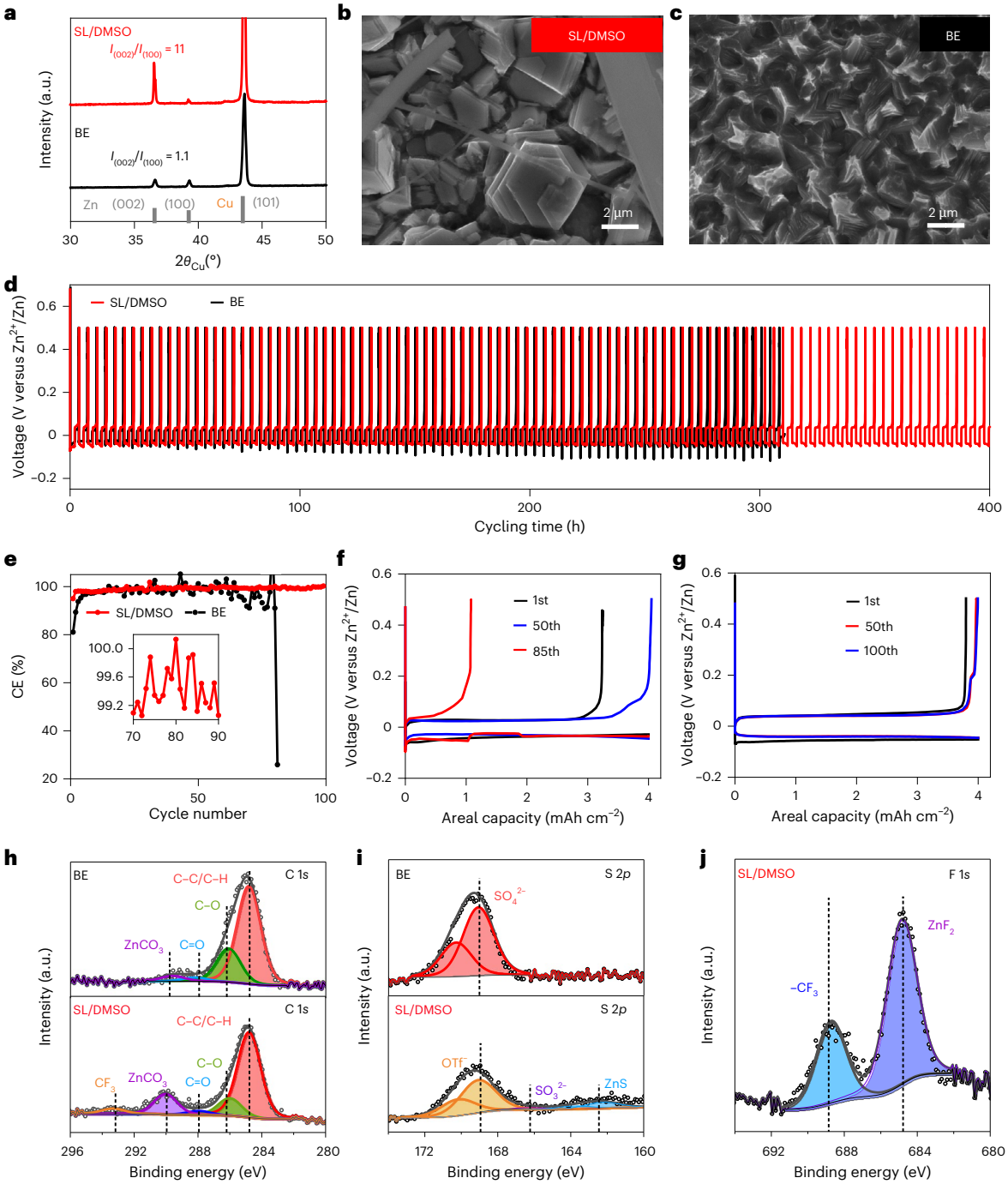


Fig. 8 | Deposition morphology and electrochemical performance of the anode. a, XRD patterns of zinc deposition on copper substrate after five cycles in $Zn^{2+}/Zn||MnO_2/Mn^{2+}$ cells with SL/DMSO and the BE. **b**,**c**, SEM images of zinc deposition in SL/DMSO (**b**) and the BE (**c**). **d**,**e**, Galvanostatic cycling profiles and CE of Zn||Cu cells in SL/DMSO (**d**) and the BE (**e**) at 2 mA cm^{-2} with a capacity of 4 mAh cm^{-2}. **f**,**g**, Voltage profiles for Zn||Cu cells with SL/DMSO (**f**) and the BE (**g**). **h**–**j**, XPS carbon 1*s* (**h**), sulfur 2*p* (**i**) and fluorine 1*s* (**j**) spectra of copper electrodes with deposited zinc after two cycles at 2 mA cm^{-2} with 4 mAh cm^{-2} in the BE and in SL/DMSO.

in DMSO-containing electrolytes and 2.5 V in 70SL versus 2.1 V in the BE. The latter is below the 2.3-V charging voltage, indicating that the OER (equation (3)) occurs in the BE during cycling. The hybrid electrolytes also showed lower HER-onset potentials, effectively suppressing side reactions and enhancing anode stability, as detailed below.

DEMS measurements confirmed suppression of both the OER and HER in the eutectic electrolytes. Figure 7f shows continuous hydrogen evolution throughout cycling in the BE, whereas only a minimal amount was detected in 70SL, and 70DMSO suppresses HER completely. Additionally, the charging process in the BE is accompanied by significant oxygen evolution, producing 15 nmol during the first cycle. In contrast, almost no oxygen evolved in 70SL and 70DMSO. Oxygen evolution was further quantified at different charging potentials (Fig. 7g). The BE cell initiated oxygen loss at 2.1 V, whereas in 70SL, OER occurred above 2.6 V and no oxygen was detected in 70DMSO up to 2.7 V, consistent with the LSV results. Interestingly, at voltages above 2.9 V, CO_2 starts to evolve in 70DMSO instead of O_2, probably due to carbon substrate corrosion (Supplementary Fig. 25).

The results show that the hybrid electrolytes remarkably increase OER overpotential by 0.8 V, demonstrating their capability to suppress electrolyte oxidation at high charging potentials. The lower degree of electrolyte decomposition prevents depletion, maintaining stable charging currents (Supplementary Fig. 26), and contributing to prolonged cycling in the hybrid systems. Notably, gas evolution during charge affects cathode surface morphology by interrupting contact between MnO_2 and the substrate, leading to active material detachment and subsequent capacity deterioration[70]. SEM images reveal irregular, patchy oxide deposition in the BE, contrasting with homogeneous, flat layers in 70SL (Supplementary Fig. 27). By suppressing gas evolution and providing optimal deposition conditions, the hybrid electrolytes improve both morphology and electrochemical performance.

Anode performance in the hybrid electrolyte

The compatibility of the hybrid electrolyte with a zinc anode was evaluated in the optimal SL/DMSO system that exhibits significant advantages over the BE. Ex situ XRD (Fig. 8a) of zinc deposition in a full cell with SL/DMSO reveals a highly textured (002)-dominated surface after five plating/stripping cycles. The $I_{(002)}/I_{(100)}$ intensity ratio reaches 11 in SL/DMSO, ten-fold higher than 1.1 in the BE. SEM images (Fig. 8b,c) show that zinc electrodeposits predominantly as flat hexagonal plates. The morphology of zinc deposits greatly influences cycling[71] and a (002)-dominant surface is favourable for suppressing the HER and dendrite growth[72,73], whereas in the BE, the zinc exhibits randomly oriented deposits with porous structures. The asymmetric Zn||Cu cell in SL/DMSO cycled over 400 h at a high areal capacity of 4 mAh cm^{-2} and a current density of 2 mA cm^{-2}, exhibiting 99.6% average CE over 100 cycles (Fig. 8d,e). In comparison, the BE experienced increased polarization and shorted after 300 h due to soft shorts and detached 'dead Zn'[74]. In contrast to the fluctuating zinc plating/stripping profiles in the BE (Fig. 8f), steady and consistent profiles in SL/DMSO were observed throughout (Fig. 8g). Additionally, the electrolyte benefits from suppressed HER and reduced layered double hydroxide formation (Supplementary Fig. 28)[75]. XPS studies at the anode surface (Fig. 8h–j and Supplementary Fig. 29) reveal a ZnS, ZnF_2-rich solid–electrolyte interphase formed in hybrid electrolytes that helps suppress the HER[76–78], whereas only zinc sulfate layered double hydroxide was formed in the BE. The galvanostatic cycling performance of Zn||Cu cells in different dual-solvent eutectic electrolytes is shown in Supplementary Figs. 30 and 31.

Conclusions

Eutectic hybrid aqueous–organic electrolytes enable highly reversible MnO_2 electrodeposition/dissolution without external acid addition. Our holistic investigation demonstrates that deep eutectic electrolytes with strong water hydrogen-bond network regulation—such as DMSO/water and SL/water—facilitate remarkably efficient MnO_2/Mn^{2+} electrochemistry at the cathode, while simultaneously enabling optimal Zn^{2+}/Zn cycling (without any HER) at the anode. The ternary electrolyte demonstrates a synergistic effect that preserves the stability of SL and phase selectivity in DMSO because it induces a unique DMSO-participating cation solvation structure. This promotes layered, poorly crystalline δ-MnO_2 (birnessite) formation with expanded interplanar spacing due to a gallery of water molecules, in contrast to dense ε-MnO_2 that lacks this open structure. In turn, this enhances proton mobility and water intrusion during cycling, enabling the rapid proton exchange necessary for efficient stripping. Notably, birnessite formation correlates with excellent cycling performance, similar to systems using surfactant additives[37], although the subtleties that govern birnessite deposition in these different electrolyte configurations remain unclear. However, in contrast to strategies using a small fraction of additives, our system remarkably suppresses the detrimental OER with a 0.8 V extended overpotential up to >2.9 V versus Zn^{2+}/Zn—well above MnO_2 deposition potential. This is important for practical applications because oxygen gas release causes rapid electrolyte depletion, pressure build-up and safety hazards[79].

Our optimized SL/DMSO ternary electrolyte achieves over 5,000 cycles with 95% CE at viable capacity. Although this strategy effectively addresses challenges for MnO_2 stripping, further improvements will expand practical applications. This work demonstrates rational electrolyte engineering for dual-electrode-free Zn^{2+}/Zn||MnO_2/Mn^{2+} batteries and provides insights that could expedite development of high-energy-density, low-cost zinc-based energy storage systems.

Methods

Electrolyte preparation and cell assembly

For the BE, 2.876 g (10 mmol) $ZnSO_4{\cdot}7H_2O$ (≥99.5%, Sigma-Aldrich) and 1.69 g (10 mmol) $MnSO_4{\cdot}H_2O$ (≥99.5%, Sigma-Aldrich) were dissolved in 10 g of Milli-Q water and stirred for 2 h. For 70SL, 7 g sulfolane (99%, Sigma-Aldrich) and 3 g Milli-Q water were mixed at 25 °C to form the 70SL solvent. For 70DMSO and 70SN, 7 g DMSO (ACS reagent, ≥99.9%, Sigma-Aldrich) and SN (99%, Sigma-Aldrich) were used, respectively. For SL/DMSO, 4 g SL and 3 g DMSO were mixed with 3 g of water. The salts, 3.635 g (10 mmol) $Zn(OTf)_2$ (98%, Sigma-Aldrich) and 0.99 g (5 mmol) $MnCl_2$ (98.0–101.0%, BDH) were added to the solvents and stirred for 2 h. For the hybrid electrolytes, $Zn(OTf)_2$ and $MnCl_2$ were chosen for their high solubility compared to $ZnSO_4$ and $MnSO_4$. The concentration was optimized based on the galvanostatic cycling performance of Zn||Cu cells.

Full Cu||GF cells were assembled in a custom cell with graphite felt as the cathode (diameter, 10 mm; thickness, 2 mm) and titanium foil as the current collector; copper foil was used as the anode current collector (diameter, 11 mm; thickness, 9 µm). The volume required for zinc deposition is 0.242 mm^3 based on the capacity of 2 mAh cm^{-2}, which is achievable in our cell design. The graphite felt provides a high surface area of 187 cm^2 per electrode, calculated by the method previously reported[80]. For the full cell, 500 µl of electrolyte was used. Asymmetric Zn||Cu cells used copper foil (diameter, 11 mm) as the positive electrode and zinc foil (99.9%; Sigma-Aldrich; diameter, 10 mm; thickness, 250 µm) as the negative electrode. The Zn||Cu cells were tested in Swagelok cells with 100 µl of electrolyte. Commercial glass fibre (Whatman; diameter, 12.7 mm) was used as the separator.

Electrochemical measurements

Galvanostatic cycling, LSV and EIS were carried out on a VMP3 potentiostat/galvanostat station (Bio-Logic) at 25 °C. The scan rate for LSV was 1 mV s^{-1}. EIS was conducted with a test voltage amplitude of 5 mV and a frequency range from 1 MHz to 100 mHz. Impedance measurements were recorded after the cell was fully discharged and rested for 10 min to reach equilibrium. For anodic LSV, graphite felt was used as the working electrode, titanium foil as the counter-electrode and zinc as the reference. Titanium foil was used as both positive and negative electrode for the cathodic scan. EIS was conducted with graphite felt as the working electrode, zinc as the counter-electrode and Ag/AgCl (3 M KCl, Sigma-Aldrich) as the reference electrode.

Characterization

High-resolution XRD measurements of the cathodes were performed at the European Synchrotron Radiation Facility on beamline ID31 (X-ray energy, ~75 keV; λ = 0.165 Å). XRD patterns of the anode were acquired on a PANalytical Empyrean with copper Kα radiation. SEM images were obtained on a Zeiss FESEM 1530. The ionic conductivities of the electrolytes were evaluated using an Orion Star A325 pH/conductivity meter (Thermo) at 23 °C. The viscosities were measured using an automated viscometer (RheoSense) at the same temperature. FTIR spectroscopy was carried out on a Bruker Tensor 27 system. Raman spectroscopy was conducted on an Oxford WITec instrument with an excitation wavelength of 532 nm. XPS spectra was obtained on a VGS ESCALab 250 Imaging ESCA instrument, and the data were fitted by

CasaXPS software, where the carbon 1*s* peak of 284.8 eV was used to calibrate the binding energies. Gaussian–Lorentzian functions and a Shirley background were used for spectral fitting. The DEMS experiment was conducted on a SpectroInlets EC-MS premium instrument to monitor gas evolution in situ. Headspace gas chromatography–mass spectrometry analysis of electrolytes after cycling was conducted on a Varian CP-3800 with a flame ionization detector. The electrolyte was heated to 100 °C and the volatile species were examined. Operando pH measurement was performed in a three-electrode Swagelok cell adapted from a previously reported cell design[69], in which a flat Xylem Blueline 27 pH electrode is attached to the electrodes to monitor the pH in situ at the electrode surface. The copper anode was perforated prior to measurement to improve contact between the electrolyte and the pH meter.

Cryo-EM sample preparation and imaging

The batteries were disassembled, and the cathodes were rinsed three times by dropping 100 ml of deionized water onto their surfaces to remove residual salts. Immediately after rinsing, the cathodes were gently scraped with a clean, fine-tipped tweezer to transfer the nanomaterials onto TEM grids, following a previous literature protocol[81]. The TEM grids were dried and then rapidly plunged into liquid nitrogen. The grids were loaded into a cryogenic grid box in a Dewar with liquid nitrogen for later imaging.

For imaging, each TEM grid was mounted onto a Gatan 626 TEM cryo-transfer holder with a built-in shutter and an attached liquid nitrogen Dewar using a cryo-transfer station. During insertion of the holder into the microscope column (~1-s exposure), the shutter remained closed to minimize exposure to ambient conditions and prevent ice condensation or loss of water from any hydrated phase (for example, birnessite) on the specimen, thereby preserving its native state. The attached Dewar ensured the specimen remained at a cryogenic temperature of around −178 °C throughout imaging. All cryo-EM characterizations were conducted using an FEI Titan 80-300 scanning transmission electron microscope operated at 300 kV and equipped with an energy-dispersive X-ray spectroscopy detector.

DFT calculations and MD simulations

See Supplementary Note 1.

Data availability

All relevant data that support the findings of this study are presented in the Article and its Supplementary Information.

References

1. Yang, C. et al. All-temperature zinc batteries with high-entropy aqueous electrolyte. *Nat. Sustain.* **6**, 325–335 (2023).
2. Fang, G., Zhou, J., Pan, A. & Liang, S. Recent advances in aqueous zinc-ion batteries. *ACS Energy Lett.* **3**, 2480–2501 (2018).
3. Tang, B., Shan, L., Liang, S. & Zhou, J. Issues and opportunities facing aqueous zinc-ion batteries. *Energy Environ. Sci.* **12**, 3288–3304 (2019).
4. Innocenti, A., Bresser, D., Garche, J. & Passerini, S. A critical discussion of the current availability of lithium and zinc for use in batteries. *Nat. Commun.* **15**, 4068 (2024).
5. Xu, C., Li, B., Du, H. & Kang, F. Energetic zinc ion chemistry: the rechargeable zinc ion battery. *Angew. Chem. Int. Ed.* **51**, 933–935 (2011).
6. Lee, B. et al. Electrochemically-induced reversible transition from the tunneled to layered polymorphs of manganese dioxide. *Sci. Rep.* **4**, 6066 (2014).
7. Hu, P. et al. Porous V_2O_5 microspheres: a high-capacity cathode material for aqueous zinc-ion batteries. *Chem. Commun.* **55**, 8486–8489 (2019).
8. Zhang, N. et al. Rechargeable aqueous Zn–V_2O_5 battery with high energy density and long cycle life. *ACS Energy Lett.* **3**, 1366–1372 (2018).
9. Zhang, L. et al. $ZnCl_2$ `water-in-salt' electrolyte transforms the performance of vanadium oxide as a Zn battery cathode. *Adv. Funct. Mater.* **29**, 1902653 (2019).
10. Li, G. et al. Developing cathode materials for aqueous zinc ion batteries: challenges and practical prospects. *Adv. Funct. Mater.* **34**, 2301291 (2024).
11. Yuan, Y. et al. Understanding intercalation chemistry for sustainable aqueous zinc–manganese dioxide batteries. *Nat. Sustain.* **5**, 890–898 (2022).
12. Blanc, L. E., Kundu, D. & Nazar, L. F. Scientific challenges for the implementation of Zn-ion batteries. *Joule* **4**, 771–799 (2020).
13. Wan, F. & Niu, Z. Design strategies for vanadium-based aqueous zinc-ion batteries. *Angew. Chem. Int. Ed.* **131**, 16508–16517 (2019).
14. Yang, H. et al. The origin of capacity fluctuation and rescue of dead Mn-based Zn–ion batteries: a Mn-based competitive capacity evolution protocol. *Energy Environ. Sci.* **15**, 1106–1118 (2022).
15. Pan, H. et al. Reversible aqueous zinc/manganese oxide energy storage from conversion reactions. *Nat. Energy* **1**, 16039 (2016).
16. Alfaruqi, M. H. et al. Electrochemically induced structural transformation in a γ-MnO_2 cathode of a high capacity zinc-ion battery system. *Chem. Mater.* **27**, 3609–3620 (2015).
17. Jung, M. S., Hoang, D., Sui, Y. & Ji, X. Impact of air exposure on the performance of the MnO_2 cathode in aqueous Zn batteries. *ACS Energy Lett.* **9**, 4316–4318 (2024).
18. Qin, Z. et al. Enabling reversible MnO_2/Mn^{2+} transformation by Al^{3+} addition for aqueous Zn–MnO_2 hybrid batteries. *ACS Appl. Mater. Interfaces* **14**, 10526–10534 (2022).
19. Ruan, P. et al. Promoting reversible dissolution/deposition of MnO_2 for high-energy-density zinc batteries via enhancing cut-off voltage. *ChemSusChem* **15**, e202201118 (2022).
20. Wang, M. et al. Opportunities of aqueous manganese-based batteries with deposition and stripping chemistry. *Adv. Energy Mater.* **11**, 2002904 (2020).
21. Fan, W. et al. Inner-sphere electron transfer enabling highly reversible Mn^{2+}/MnO_2 conversion toward energy-dense electrolytic zinc–manganese batteries. *J. Am. Chem. Soc.* **147**, 18694–18703 (2025).
22. Chen, H. et al. Achieving highly reversible Mn^{2+}/MnO_2 conversion reaction in electrolytic Zn-MnO_2 batteries via electrochemical–chemical process regulation. *Angew. Chem. Int. Ed.* **64**, e202423999 (2025).
23. Mateos, M., Makivic, N., Kim, Y., Limoges, B. & Balland, V. Accessing the two-electron charge storage capacity of MnO_2 in mild aqueous electrolytes. *Adv. Energy Mater.* **10**, 2000332 (2020).
24. Aguilar, I. et al. Identifying interfacial mechanisms limitations within aqueous Zn–MnO_2 batteries and means to cure them with additives. *Energy Storage Mater.* **53**, 238–253 (2022).
25. Ye, X. et al. Unraveling the deposition/dissolution chemistry of MnO_2 for high-energy aqueous batteries. *Energy Environ. Sci.* **16**, 1016–1023 (2023).
26. Chao, D. et al. An electrolytic Zn–MnO_2 battery for high-voltage and scalable energy storage. *Angew. Chem. Int. Ed.* **131**, 7905–7910 (2019).
27. Chen, W. et al. A manganese–hydrogen battery with potential for grid-scale energy storage. *Nat. Energy* **3**, 428–435 (2018).
28. Liang, G. et al. A universal principle to design reversible aqueous batteries based on deposition–dissolution mechanism. *Adv. Energy Mater.* **9**, 1901838 (2019).

29. Huang, J. et al. Low-cost and high safe manganese-based aqueous battery for grid energy storage and conversion. *Sci. Bull.* **64**, 1780–1787 (2019).
30. Singh, A. et al. Towards a high MnO_2 loading and gravimetric capacity from proton-coupled Mn^{4+}/Mn^{2+} reactions using a 3D free-standing conducting scaffold. *J. Mater. Chem. A* **9**, 1500–1506 (2021).
31. Mateos, M., Harris, K. D., Limoges, B. & Balland, V. Nanostructured electrode enabling fast and fully reversible MnO_2-to-Mn^{2+} conversion in mild buffered aqueous electrolytes. *ACS Appl. Energy Mater.* **3**, 7610–7618 (2020).
32. Zhong, C. et al. Decoupling electrolytes towards stable and high-energy rechargeable aqueous zinc–manganese dioxide batteries. *Nat. Energy* **5**, 440–449 (2020).
33. Li, G. Membrane-free Zn/MnO_2 flow battery for large-scale energy storage. *Adv. Energy Mater.* **10**, 1902085 (2020).
34. Dai, L. et al. Jahn–teller distortion induced Mn^{2+}-rich cathode enables optimal flexible aqueous high-voltage zn-mn batteries. *Adv. Sci.* **8**, 2004995 (2021).
35. Wang, Y. et al. Cation-regulated MnO_2 reduction reaction enabling long-term stable zinc–manganese flow batteries with high energy density. *Energy Environ. Sci.* **18**, 1524–1532 (2025).
36. Zeng, X. et al. Toward a reversible Mn^{4+}/Mn^{2+} redox reaction and dendrite-free Zn anode in near-neutral aqueous Zn/MnO_2 batteries via salt anion chemistry. *Adv. Energy Mat.* **10**, 1904163 (2020).
37. Li, Y. et al. In situ formation of liquid crystal interphase in electrolytes with soft templating effects for aqueous dual-electrode-free batteries. *Nat. Energy* **9**, 1350–1359 (2024).
38. Sheng, D. et al. Hydrogen bond network regulation in electrolyte structure for Zn-based aqueous batteries. *Adv. Funct. Mater.* **34**, 2402014 (2024).
39. Liu, S. et al. Tuning the electrolyte solvation structure to suppress cathode dissolution, water reactivity, and Zn dendrite growth in zinc-ion batteries. *Adv. Funct. Mater.* **31**, 2104281 (2021).
40. Miao, L. et al. Aqueous electrolytes with hydrophobic organic cosolvents for stabilizing zinc metal anodes. *ACS Nano* **16**, 9667–9678 (2022).
41. Li, C. et al. Enabling selective zinc-ion intercalation by a eutectic electrolyte for practical anodeless zinc batteries. *Nat. Commun.* **14**, 3067 (2023).
42. Wang, Y. et al. Sulfolane-containing aqueous electrolyte solutions for producing efficient ampere-hour-level zinc metal battery pouch cells. *Nat. Commun.* **14**, 1828 (2023).
43. Yang, W. et al. Hydrated eutectic electrolytes with ligand-oriented solvation shells for long-cycling zinc–organic batteries. *Joule* **4**, 1557–1574 (2020).
44. Geng, L. et al. Eutectic electrolyte with unique solvation structure for high-performance zinc-ion batteries. *Angew. Chem. Int. Ed.* **61**, e202206717 (2022).
45. Cao, L. et al. Solvation structure design for aqueous Zn metal batteries. *J. Am. Chem. Soc.* **142**, 21404–21409 (2020).
46. Shi, J. et al. 'Water-in-deep eutectic solvent' electrolytes for high-performance aqueous Zn-ion batteries. *Adv. Funct. Mater.* **31**, 2102035 (2021).
47. Deng, Y. et al. Nanomicellar electrolyte to control release ions and reconstruct hydrogen bonding network for ultrastable high-energy-density Zn–Mn battery. *J. Am. Chem. Soc.* **145**, 20109–20120 (2023).
48. Carlson, E. Z., Chueh, W. C., Mefford, J. T. & Bajdich, M. Selectivity of electrochemical ion insertion into manganese dioxide polymorphs. *ACS Appl. Mater. Interfaces* **15**, 1513–1524 (2022).
49. Kim, C.-H. et al. The structure and ordering of ε-MnO_2. *J. Solid State Chem.* **179**, 753–774 (2006).
50. Gao, P. et al. The critical role of point defects in improving the specific capacitance of δ-MnO_2 nanosheets. *Nat. Commun.* **8**, 14559 (2017).
51. Zhang, Q. et al. Unveiling the energy storage mechanism of MnO_2 polymorphs for zinc–manganese dioxide batteries. *Adv. Funct. Mater.* **34**, 2306652 (2024).
52. Li, Z. et al. Localized water restriction in ternary eutectic electrolytes for ultra-low temperature hydrogen batteries. *Angew. Chem. Int. Ed.* **64**, e202416800 (2025).
53. Chuai, M. et al. Theory-driven design of a cationic accelerator for high-performance electrolytic MnO_2–Zn batteries. *Adv. Mater.* **34**, 2203249 (2022).
54. Zuo, Y. et al. Boosted H^+ intercalation enables ultrahigh rate performance of the δ-MnO_2 cathode for aqueous zinc batteries. *ACS Appl. Mater. Interfaces* **14**, 26653–26661 (2022).
55. Boyd, S. et al. Effects of interlayer confinement and hydration on capacitive charge storage in birnessite. *Nat. Mater.* **20**, 1689–1694 (2021).
56. Chao, D. et al. Amorphous VO_2: a pseudocapacitive platform for high-rate symmetric batteries. *Adv. Mater.* **33**, 2103736 (2021).
57. Balachandran, D., Morgan, D. & Ceder, G. First principles study of H-insertion in MnO_2. *J. Solid State Chem.* **166**, 91–103 (2002).
58. Xiao, X. et al. Ultrahigh-loading manganese-based electrodes for aqueous batteries via polymorph tuning. *Adv. Mater.* **35**, 2211555 (2023).
59. Zhang, Y. et al. Amorphization stabilizes Te-based aqueous batteries via confining free water. *Angew. Chem. Int. Ed.* **64**, e202424056 (2025).
60. Song, Z. et al. Anionic co-insertion charge storage in dinitrobenzene cathodes for high-performance aqueous zinc–organic batteries. *Angew. Chem. Int. Ed.* **61**, e202208821 (2022).
61. Yun, S.-H. et al. Solvate structures and computational/spectroscopic characterization of $LiCF_3SO_3$ e. *J. Phys. Chem. C* **126**, 18251–18265 (2022).
62. Wang, F. et al. Highly reversible zinc metal anode for aqueous batteries. *Nat. Mater.* **17**, 543–549 (2018).
63. Wang, Y. et al. Solvent control of water O–H bonds for highly reversible zinc ion batteries. *Nat. Commun.* **14**, 2720 (2023).
64. Cao, J. et al. Strategies of regulating Zn^{2+} solvation structures for dendrite-free and side reaction suppressed zinc-ion batteries. *Energy Environ. Sci.* **15**, 499–528 (2022).
65. Ren, Y., Li, H., Rao, Y., Zhou, H. & Guo, S. Aqueous MnO_2/Mn^{2+} electrochemistry in batteries: progress, challenges, and perspectives. *Energy Environ. Sci.* **17**, 425–441 (2024).
66. Chuai, M. et al. High-performance Zn battery with transition metal ions co-regulated electrolytic MnO_2. *eScience* **1**, 178–185 (2021).
67. Aguilar, I. et al. A key advance toward practical aqueous Zn/MnO_2 batteries via better electrolyte design. *Joule* **9**, 101784 (2025).
68. Li, M. et al. Comprehensive H_2O molecules regulation via deep eutectic solvents for ultra-stable zinc metal anode. *Angew. Chem. Int. Ed.* **62**, e202215552 (2023).
69. Liu, X. et al. Operando pH measurements decipher H^+/Zn^{2+} intercalation chemistry in high-performance aqueous Zn/δ-V_2O_5 batteries. *ACS Energy Lett.* **5**, 2979–2986 (2020).
70. Pu, S. D. et al. Decoupling, quantifying, and restoring aging-induced Zn-anode losses in rechargeable aqueous zinc batteries. *Joule* **7**, 366–379 (2023).
71. Zhang, Y. et al. Separator effect on zinc electrodeposition behavior and its implication for zinc battery lifetime. *Nano Lett.* **21**, 10446–10452 (2021).
72. Zhou, M. et al. Surface-preferred crystal plane for a stable and reversible zinc anode. *Adv. Mater.* **33**, 2100187 (2021).
73. Zheng, J. et al. Reversible epitaxial electrodeposition of metals in battery anodes. *Science* **366**, 645–648 (2019).

74. Li, Q., Chen, A., Wang, D., Pei, Z. & Zhi, C. 'Soft shorts' hidden in zinc metal anode research. *Joule* **6**, 273–279 (2022).
75. Oberholzer, P., Tervoort, E., Bouzid, A., Pasquarello, A. & Kundu, D. Oxide versus nonoxide cathode materials for aqueous Zn batteries: an insight into the charge storage mechanism and consequences thereof. *ACS Appl. Mater. Interfaces* **11**, 674–682 (2018).
76. Cao, L. et al. Fluorinated interphase enables reversible aqueous zinc battery chemistries. *Nat. Nanotechnol.* **16**, 902–910 (2021).
77. Li, M. et al. Trace sulfonic acid additives modulate Zn^{2+} transport through sei and desolvation for highly reversible zinc anodes. *Small* **21**, 2503002 (2025).
78. Li, C. et al. Highly reversible Zn anode with a practical areal capacity enabled by a sustainable electrolyte and superacid interfacial chemistry. *Joule* **6**, 1103–1120 (2022).
79. Suo, L. et al. 'Water-in-salt' electrolyte enables high-voltage aqueous lithium-ion chemistries. *Science* **350**, 938–943 (2015).
80. Smith, R. E. G., Davies, T. J., Baynes, N. de & Nichols, R. J. The electrochemical characterisation of graphite felts. *J. Electroanal. Chem.* **747**, 29–38 (2015).
81. Zhang, Z. et al. Cathode–electrolyte interphase in lithium batteries revealed by cryogenic electron microscopy. *Matter* **4**, 302–312 (2021).

Acknowledgements

This work was supported by the NSERC through funds to L.F.N. via the Discovery Grant and Canada Research Chair programmes. Modelling at ARL was supported by the US Department of Energy via SN2020957. We thank the Aqueous Battery Consortium (ABC) for inspiration for this work, and Z. Yu, and Y. Wang for assistance with the DSC and XRD measurements. We appreciate valuable discussions held with V. Augustyn, R. Clement and T. P. Pollard during the course of the work.

Author contributions

C.L. and L.F.N. designed this study. J.L. carried out the characterization and all the electrochemical measurements. B.L. performed TEM and STEM-EDS studies. Y.L. supervised the TEM studies. O.B. performed DFT calculations and MD simulations. J.L., C.L. and L.F.N. wrote the manuscript with contributions from other authors.

Competing interests

The authors declare no competing interests.

Additional information

Supplementary information The online version contains supplementary material available at https://doi.org/10.1038/s41560-025-01958-8.

Correspondence and requests for materials should be addressed to Chang Li or Linda F. Nazar.

Peer review information *Nature Energy* thanks Christel Laberty-Robert, Jinwoo Lee and Yuqi Li for their contribution to the peer review of this work.

Reprints and permissions information is available at www.nature.com/reprints.

Publisher's note Springer Nature remains neutral with regard to jurisdictional claims in published maps and institutional affiliations.

Springer Nature or its licensor (e.g. a society or other partner) holds exclusive rights to this article under a publishing agreement with the author(s) or other rightsholder(s); author self-archiving of the accepted manuscript version of this article is solely governed by the terms of such publishing agreement and applicable law.

© The Author(s), under exclusive licence to Springer Nature Limited 2026